A Novel Disturbance Device for Aerial Manipulation Experiments

Benjamin James Marshall, James Knowles, Yunda Yan, Cunjia Liu
Department of Aeronautical and Automotive Engineering
Loughborough University
Loughborough, United Kingdom, LE11 3TU
{b.marshall, j.a.c.knowles, y.yan, c.liu5}@lboro.ac.uk

***Abstract*—In the last decade, UAVs endowed with manipulators have increased in their ability to complete complex tasks such as manipulating doors and drawers. Very recent work also includes tasks with non-constant dynamics such as pushing a cart along a surface with a change in friction coefficient or pulling an electrical plug from a socket. These tasks are hard to design and compare controllers for because their dynamics are complex and they may not behave consistently. This paper proposes a tunable and repeatable mechanism for use in experiments that compare different controller designs. The proposed mechanism, called an overcentre mechanism, can provide a nonlinear resistive force and can be easily modified for different force magnitudes. Additionally, it can be quickly re-oriented to disturb altitude or position channels for vehicles with or without manipulators. This paper experimentally compares three traditional observer designs and a baseline controller in two different operating conditions.**

***Index Terms*—Aerial manipulator, environmental interaction, observer design**

I. Introduction

Using an aerial robot to interact with an object has been widely studied in the past 5 years. Aerial systems have expanded their capabilities from picking up simple objects [1], [10], [3];to manipulating simple known mechanisms (eg doors [8], drawers [6]); to manipulating systems with switched dynamics. These switched systems could include sliding objects with non-constant friction [2]; pulling an electrical plug out of a socket [4]; and autonomous removal of a sensor mounted with adhesive [5]. In addition to this, sustained-contact is currently under research, with applications to aerial writing [13] and UAV-based cleaning [11], [14].

To develop these capabilities, existing work applies robust control techniques such as Disturbance Observer Based (DOB) Control [4], Model Predictive Control [8] and Model Reference Adaptive Control [1]. For cases in which the vehicle does not start attached to the manipulation object, controllers also typically make use of a high level controller such as a Finite State Machine or Hybrid Automata [4]. In the aforementioned tasks, the dynamics of the robot-environment interaction are inconsistent. The manipulation task may not provide repeatable disturbances or their disturbance profile may be hard to characterise, additionally, it may be nontrivial to adjust their disturbance profile for robustness assessment, or comparison of multiple controllers.

This presents a problem for engineers seeking to compare different control methodologies in these applications, as a statistically significant volume of data must be captured to prove that a given controller is superior. This paper presents a mechanism which can act as a repeatable analogue to switched disturbances in industrial applications. This mechanism, known as an overcentre mechanism, provides a disturbance which resists movement until a particular force threshold has been met, after which it suddenly dissipates. This is similar to many modern aerial-environmental interaction tasks, such as retrieving a box from inside a cluttered container. The mechanism can also easily be modified to change the disturbance force magnitude [7], and the speed of the switch. This allows practitioners to make a mechanical analogue to their real system and easily compare a number of different controllers against each other without a large volume of testing data. This paper goes on to experimentally test three popular observer designs on a HexSoon 450 size quadcopter. Each observer is tested attached to the overcentre mechanism in a low-force operating condition and in a second high-force operating condition.

II. Problem Formulation

In the following section, the dynamics of the vehicle will be introduced and linearised. The assumptions made for the experiments in this paper are then discussed. Consider the nonlinear dynamics of the quadcopter as follows:

$$\begin{cases} \ddot{x} = \frac{U(\mathrm{c}(\psi)\mathrm{c}(\theta)\mathrm{c}(\phi)+\mathrm{s}(\psi)\mathrm{s}(\phi))}{m} + \frac{d_x}{m} \\ \ddot{y} = \frac{U(\mathrm{s}(\psi)\mathrm{s}(\theta)\mathrm{c}(\phi)-\mathrm{c}(\psi)\mathrm{s}(\theta))}{m} + \frac{d_y}{m} \\ \ddot{z} = g - \frac{U\mathrm{c}(\phi)\mathrm{c}(\theta)}{m} + \frac{d_z}{m} \\ \ddot{\phi} = \frac{\tau_\phi}{I_{xx}} + \frac{\dot{\theta}\dot{\psi}(I_{yy}-I_{zz})}{I_{xx}} \\ \ddot{\theta} = \frac{\tau_\theta}{I_{yy}} + \frac{\dot{\phi}\dot{\psi}(I_{zz}-I_{xx})}{I_{yy}} \\ \ddot{\psi} = \frac{\tau_\psi}{I_{zz}} + \frac{\dot{\phi}\dot{\theta}(I_{xx}-I_{yy})}{I_{zz}} \end{cases} \tag{1}$$

where $x, y, z \in \mathbb{R}$ are the positions of the drone centre of gravity in the inertial reference frame as shown in Fig. 1. The angles $\phi, \theta, \psi \in \mathbb{R}$ are the body roll, pitch, and yaw angles. In the full nonlinear model, disturbance forces in the inertial frame are $d_x, d_y, d_z \in \mathbb{R}$. Controls are considered as total thrust $U \in \mathbb{R}_+$ and torque about each body-axis $\tau_\phi, \tau_\theta, \tau_\psi \in \mathbb{R}$. $I_{xx}, I_{yy}, I_{zz} \in \mathbb{R}_+$ are the moments of inertia about each body-axis. The vehicle mass is given by $m \in \mathbb{R}_+$. In the above, c() and s() are shorthand for sine and cosine functions.

Acceleration due to gravity is given by $g \in \mathbb{R}_+$. In these initial experiments, the controllers and observers each use linearized models where $\phi, \theta \approx 0$. It is also assumed that the drone is vertically above the overcentre mechanism, and that the vector between the drone and overcentre is approximately parallel to z, hence d_x and $d_y \approx 0$. Additionally, they assume that the inner loop controller and dynamics are desirable. This gives two linearized models:

$$\begin{bmatrix} \ddot{x} \\ \ddot{y} \end{bmatrix} = g \begin{bmatrix} \mathrm{c}(\psi) & -\mathrm{s}(\psi) \\ \mathrm{s}(\psi) & \mathrm{c}(\psi) \end{bmatrix} \begin{bmatrix} 0 & -1 \\ 1 & 0 \end{bmatrix} \begin{bmatrix} \phi \\ \theta \end{bmatrix} \tag{2}$$

$$\ddot{z} = g + \frac{d_z - U}{m} \tag{3}$$

The state-space model of (3) is:

$$\underbrace{\begin{bmatrix} \dot{z} \\ \ddot{z} \end{bmatrix}}_{\dot{X}} = \underbrace{\begin{bmatrix} 0 & 1 \\ 0 & 0 \end{bmatrix}}_{A} \underbrace{\begin{bmatrix} z \\ \dot{z} \end{bmatrix}}_{X} + \underbrace{\begin{bmatrix} 0 \\ \frac{1}{m} \end{bmatrix}}_{B} (g - U + d_z) \tag{4}$$

III. Generating a Disturbance

In practice, generating a tunable disturbance in the real world is challenging. To create this we use a mechanism called an Overcentre mechanism. The key geometry and behaviour of this mechanism will be discussed next.

A. The Overcentre Mechanism

The overcentre mechanism is formed of two links connected by a revolute joint. The left-hand link is rigidly pinned to the origin, the right-hand link is bound by a prismatic joint to the xy plane (shown in Fig. 1). A spring connects the midpoint of each link. This creates a mechanism with three equilibria.

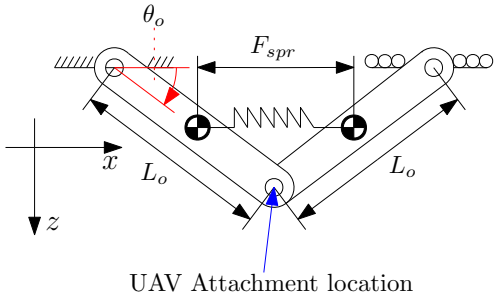

Fig. 1: Overcentre mechanism free body diagram and inertial frame.

Two equilibria are stable – with the links down, and the links up; the third equilibria with the links level is unstable. As a load is applied to the centre joint, the links will not move until a particular force threshold is met, at which time the links will "snap" from one equilibria to another. In this case, the overcentre mechanism is initialised with the links down. The translation of the right hand joint is bound by $y = 0$ and $|x_o| \leq 2L_o\mathrm{c}(|\theta_o|)$. $x_o \in \mathbb{R}$ is the x co-ordinate of the right-hand joint of the overcentre mechanism. $L_o \in \mathbb{R}$ is the length of each link, and $\theta_o \in \mathbb{R}$ is the angle between the x_+ axis and the left-hand link of the mechanism. The force required to hold the mechanism at a particular position is given by:

$$F = 2K\tan(\theta)(L_o\mathrm{c}(\theta_o) - l_{us}) \tag{5}$$

where $F \in \mathbb{R}$ is the force required at the centre joint; $K \in \mathbb{R}_+$ is the spring coefficient; and $l_{us} \in \mathbb{R}_+$ is the unstrained length of the spring. These can all be adjusted by the user to obtain different disturbance profiles for a range of applications. The UAV centre of gravity is then attached by a bungee to the centre joint of the overcentre mechanism and tasked to smoothly manipulate the mechanism from the links-down state to the links-up state.

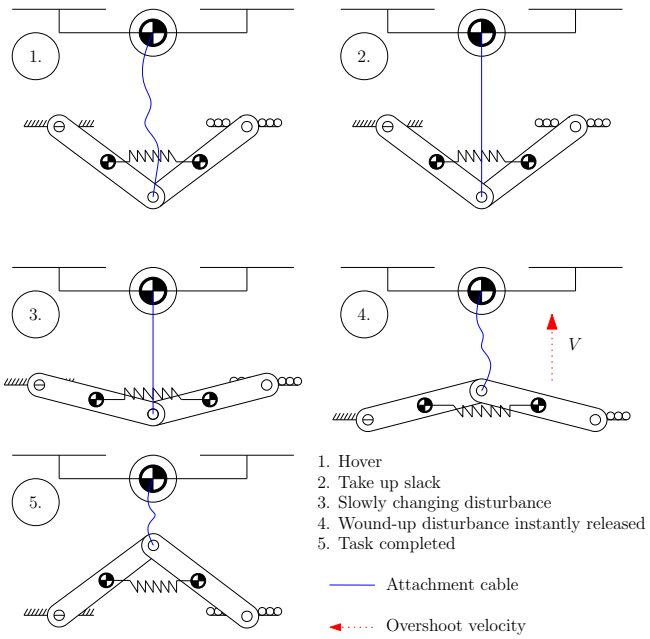

Fig. 2: Key phases of overcentre manipulation.

The use of the mechanism allows the operator to easily tune the resistance force, whilst also being more repeatable than similar disturbances. Key stages of the manipulation task are shown in Fig. 2. In stage 1, the vehicle obtains a stable hover above the mechanism. At stage 2, the ramp reference signal causes the drone to rise, the drone may be unable to meet the reference signal due to the cable attachment becoming taut. In stage 3, the static friction and resistance force of the overcentre is exceeded by the thrust of the drone, causing the mechanism to begin to move. As the links-level equilibria becomes the most attractive, the links now move of their own accord and "snap" to the other side of the links-level position. This is shown in stage 4. As the disturbance force has suddenly been released, this causes an overshoot velocity in the vertical direction that the controller should aim to mitigate. After the overcentre has snapped, the drone is then tasked to return to a stable hover above the mechanism, this is shown in stage 5.

B. Manipulation Task

In this paper, the drone is tasked to smoothly manipulate the mechanism from a links-down equilibria to a links-up

equilibria. To acheive this, a ramp signal in $z-$ is sent to the vehicle. In these early experiments, the overcentre is situated at $\begin{bmatrix} x & y \end{bmatrix}^T = 0$. Note that the location and rotation of the overcentre can be changed to excite attitude and translation channels. In the below, $h_0 \in \mathbb{R}$ is the initial height of the system, determined by the physical size of the overcentre mechanism and the length of the bungee between the UAV and mechanism. The components of the reference signal are given in the inertial frame as $r_x, r_y, r_z \in \mathbb{R}$ respectively. For initial experiments $t_{ramp} = 20s$. The reference $r \in \mathbb{R}^{3\times 1}$ is described in the inertial frame component-wise by the following.

$$r_z = \begin{cases} h_0 & t \leq t_{eq} \\ h_0 + (2L_o \mathrm{s}(|\theta_o|)) \left(\frac{t-t_{eq}}{t_{ramp}}\right) & t_{eq} < t \leq t_{ramp} + t_{eq} \\ h_0 + 2L_o \mathrm{s}(|\theta_o|) & t \geq t_{final} \end{cases} \tag{6}$$

$$r_x = r_y = 0 \tag{7}$$

IV. Controller and Observer Designs

To attempt to mitigate the influence of a disturbance, tracking error integrators (PID) and observer based compensations are popular. Here a PID controller and three observers are formulated and compared.

A. Baseline Controller

For initial experiments, the manipulation task is conducted in the altitude channel only. As a result of this, the position controller is a simple PD controller given by:

$$e_p = \begin{bmatrix} r_x & r_y \end{bmatrix}^T - \begin{bmatrix} x & y \end{bmatrix}^T \tag{8}$$

$$\begin{bmatrix} \phi \\ \theta \end{bmatrix} = \frac{1}{g} \begin{bmatrix} \mathrm{c}(\psi) & \mathrm{s}(\psi) \\ -\mathrm{s}(\psi) & \mathrm{c}(\psi) \end{bmatrix} \begin{bmatrix} 0 & 1 \\ -1 & 0 \end{bmatrix} \left(\begin{bmatrix} K_{pp} & 0 \\ 0 & K_{pp} \end{bmatrix} e_p + \begin{bmatrix} K_{pd} & 0 \\ 0 & K_{pd} \end{bmatrix} \dot{e}_p \right) \tag{9}$$

where $e_p \in \mathbb{R}^{2\times 1}$ is the position error, and $K_{pp}, K_{pd} \in \mathbb{R}_+$ are the position controller gains. Now consider the altitude dynamics given by (3) Let the altitude error be described by:

$$e_z = r_z - z \tag{10}$$

Therefore, let the baseline controller thrust command U be defined by:

$$U_{baseline} = K_{ap} e_z + K_{ad} \dot{e}_z \tag{11}$$

where each $K_{ap}, K_{ad} \in \mathbb{R}_+$ are the altitude controller gains and $U_{baseline} \in \mathbb{R}_+$ is the commanded thrust. Each observer calculates a new input U including the estimated disturbance. Thrust commands must then be converted to throttle commands $u \in \mathbb{R}, 0 \leq u \leq 1$. An experimentally found quadratic is used to map U to u, this is discussed in Sec. V-A. By assuming $\dot{r} = \ddot{r} = 0$ and that the selected observer error converges faster than the controller, the error dynamics of the controller can be described by:

$$0 = \begin{bmatrix} -K_{pp} & 0 \\ 0 & K_{pp} \end{bmatrix} e_p + \begin{bmatrix} K_{pd} & 0 \\ 0 & K_{pd} \end{bmatrix} \dot{e}_p + \ddot{e}_p \tag{12}$$

which is stable if the values of K_{pd} and K_{pp} are chosen appropriately.

B. Extended State Observer

Consider the altitude dynamics given in (3) where the disturbance is considered an additional state to obtain:

$$\begin{bmatrix} \dot{z} \\ \ddot{z} \\ \dddot{z} \end{bmatrix} = \begin{bmatrix} A_{2\times 2} & B_{2\times 1} \\ 0_{1\times 2} & 0 \end{bmatrix} \begin{bmatrix} z \\ \dot{z} \\ \ddot{z} \end{bmatrix} + \begin{bmatrix} B \\ 0 \end{bmatrix} (g - U) \tag{13}$$

where the estimated altitude, velocity and acceleration are given by $z_1, z_2, z_3 \in \mathbb{R}$ respectively. Let the error between the measured altitude z and estimated position $\tilde{z}$ be given by $\tilde{z} \in \mathbb{R}$.

$$\begin{bmatrix} \dot{z}_1 \\ \dot{z}_2 \\ \dot{z}_3 \end{bmatrix} = \begin{bmatrix} A_{2\times 2} & B_{2\times 1} \\ 0_{1\times 2} & 0 \end{bmatrix} \begin{bmatrix} z_1 \\ z_2 \\ z_3 \end{bmatrix} + \begin{bmatrix} B \\ 0 \end{bmatrix} (g - U) + L_e \tilde{z} \tag{14}$$

The matrix $L_e \in \mathbb{R}^{3\times 1}$ is a gain matrix. The estimated acceleration $\ddot{\hat{z}}$ is compensated for with the following equation, where $U_{baseline}$ is produced by (11).

$$U = U_{baseline} - (z_3 + g)m \tag{15}$$

The error dynamics of the extended state observer are governed by the eigenvalues of $A - L_e C$ which are stable if $A - L_e C$ is Hurwitz.

C. Higher Order Sliding Mode Observer

The final selected observer is a Higher Order Sliding Mode Observer [12]. This observer can converge to zero estimation error within a finite time. Additionally, the ability to estimate the rate of change of the disturbance force may allow this observer to perform well in this application, especially when the operating point is changed. The observer takes the form of:

$$\begin{cases} \dot{z}_1 = z_2 + K_{s1} |\tilde{z}|^{\frac{2}{3}} \mathrm{sign}(\tilde{z}) \\ \dot{z}_2 = z_3 + K_{s2} |\tilde{z}|^{\frac{1}{3}} \mathrm{sign}(\tilde{z}) + \frac{g-U}{m} \\ \dot{z}_3 = K_{s3} \mathrm{sign}(\tilde{z}) \end{cases} \tag{16}$$

where $\tilde{z} = \hat{z} - z$ is the state estimation error. Estimated disturbances are compensated in the following way:

$$U = U_{baseline} - (z_3 + g)m \tag{17}$$

Stability of this observer is shown in [12]. Now define each estimation error as $\tilde{z}_1 = z - z_1$,$\tilde{z}_2 = \dot{z} - z_2$ and $\tilde{z}_3 = \ddot{z} - z_3$, this gives the SMO error dynamics as:

$$\begin{cases} \dot{\tilde{z}}_1 = \tilde{z}_2 - K_{s1} |\tilde{z}|^{2/3} \mathrm{sign}(\tilde{z}) \\ \dot{\tilde{z}}_2 = \tilde{z}_3 - K_{s2} |\tilde{z}|^{1/3} \mathrm{sign}(\tilde{z}) + \frac{g-U}{m} \\ \dot{\tilde{z}}_3 = -K_{s3} \mathrm{sign}(\tilde{z} + \dot{d}_z) \end{cases} \tag{18}$$

which is stable if $\dot{d}_z \leq K_{s3} \mathrm{sign}(\tilde{z})$. Further details can be found in [9]

D. Disturbance Observer

Other observers considered in this paper are driven by error between the measured altitude z and estimated altitude $\hat{z}$. The disturbance observer derived next assumes that all system states are available. This may improve performance as the velocity estimation used to estimate disturbance forces is not susceptible to poorly tuned controller gains. Consider a linear disturbance observer formulated as:

$$\begin{cases} \dot{Z} = -L_d B(Z + L_d X) - L_d(AX + BU) \\ \hat{d}_z = Z + L_d X \end{cases} \tag{19}$$

where $Z \in \mathbb{R}$ is the internal variable of the DOB, and $L_d \in \mathbb{R}^{1\times 2}$ is the observer gain to be selected. The estimated disturbance is then compensated for with:

$$U = U_{baseline} - \hat{d}_z - mg \tag{20}$$

The error dynamics of the disturbance observer are given by:

$$\dot{e}_d = -L_d B e + \dot{d}_z \tag{21}$$

where $e_d \in \mathbb{R}$ is the disturbance estimation error $d_z - \hat{d}_z$. The value of e_d is asymptotically stable if $L_d \in \mathbb{R}_+$ and $\dot{d}_z \approx 0$.

V. Experimental Testing and Results

The next section of this paper details the experimental setup, alongside the quadcopter hardware and systems. Included in this is the controller bock diagram and the two operating conditions of the overcentre mechanism. After this, the experimental results for the manipulation task detailed in Sec. III-B are presented and discussed.

A. Experimental Setup

Presented below is the controller block diagram for each controller on the real vehicle. The vehicle accepts throttle commands from zero to one, whereas each observer is formulated with forces and accelerations. To account for this, the drone throttle has been recorded with different attached masses to create a lookup table for thrust at a given throttle command. The inverse transformation is applied after the observer. The controller block diagram is shown in Fig. 3.

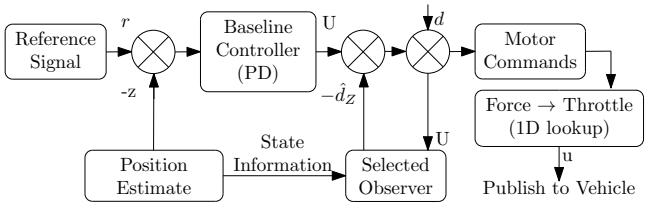

Fig. 3: Controller block diagram including transformation from throttle channel to estimated motor thrust. $\hat{d}_U$ and $\hat{d}$ is the estimated disturbance in the throttle (0-1) and force (Newtons) respectively.

Each algorithm is implemented in Simulink and compiled to a C++ ROS node. The node is then run on the on-board computer which receives external states from a VICON system by Wi-Fi. The quadcopter used in these experiments is a 450 size HexSoon Edu V2, equipped with a PixHawk Cube Black 2.1. An Intel i5-NUC is used to run on-board algorithms and publishes commands at 50 Hz. Experiments are performed indoors using a VICON motion capture system. The flying weight of the UAV is 1.87 kg.

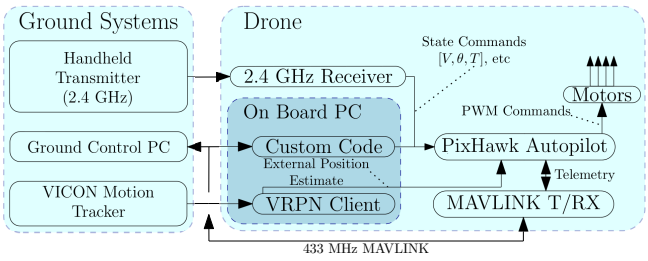

Fig. 4: Experimental systems diagram showing on board hardware and interaction with on board computer.

The physical overcentre mechanism is manufactured with $L = 200$mm and $|\theta_o| = 30°$. The spring constant is $K_{spr} = 0.10$N/mm. Smooth contact surfaces and bearings are used where relevant to reduce the influence of friction. A second operating point is also considered with $L = 200mm$, $|\theta_o| = 45°$ and $K_{spr} = 0.15$N/mm to assess robustness. To attach the drone to the overcentre mechanism, a bungee is used. For the first operating point a weak bungee is used $K_{bungee} = 20$N/M, in the second operating point a stiff bungee is used with $K_{bungee} = 65$N/M. Each of these operating points is simulated in MathWorks SimScape to demonstrate the ability to tune the actuation force of the mechanism. In the simulation, both operating conditions of the mechanism are subject to a steady ramp force in the $z-$ axis at the centre joint of the mechanism. This is shown in orange. The response of each mechanism is shown in blue, the low-force operating point snaps at 5.4 seconds. The high-force operating point snaps at 38 seconds.

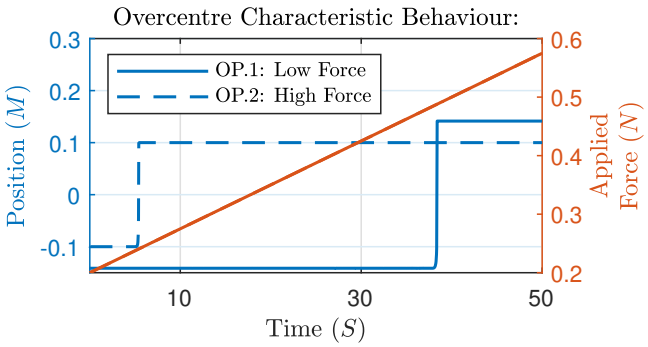

Fig. 5: Simulated overcentre mechanism at two different operating conditions.

The experimental setup and CAD design of the mechanism are shown below. Hard stops are inserted into the prismatic joint slot to determine the range of motion of the mechanism. Note that the mechanism can also be rotated about its length (x axis) to mimic a wall-attached object.

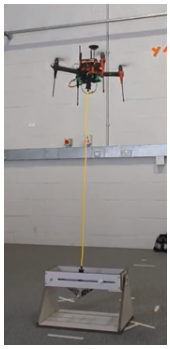

(a) UAV attached to mechanism.

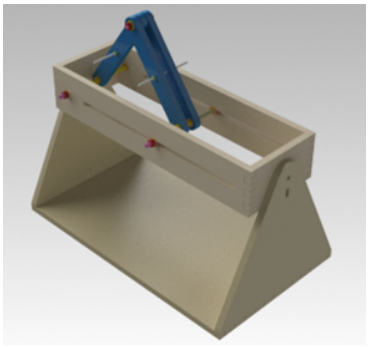

(b) Overcentre mechanical design.

Fig. 6: Experimental setup and CAD model used for initial experiments.

B. Results

In Fig. 7, the z position of the drone is shown relative to the initial position h_0, test results under the first operating point (low force) are shown in the top subplot. Tabulated results of mean square error and maximum error are shown below.

Controller	MSE ($1000 \times M^2$)	Maximum error (M)
Operating Point 1 - Low Force		
ESO	0.566	0.113
SMO	0.549	0.113
DOB	**0.266**	**0.0883**
PID	1.58	0.0810
Operating Point 2 - High Force		
ESO	3.366	0.302
SMO	2.587	0.257
DOB	**1.607**	**0.245**
PID	6.036	0.145

TABLE I: Mean Squared Error and maximum error for each observer. PID maximum error results are not considered satisfactory due to poor tracking performance

For the first operating point the PID controller, plotted with a green line, shows degraded tracking performance compared to ADRC techniques ($15 < t < 35$). PID results also show the lowest overshoot of the tested controllers. However, this reduced overshoot is due to the overcentre snap taking place later than other designs. When the PID controller overshoots at 30 seconds, the reference signal is physically higher. This masks the overshoot performance of this controller. The PID controller does not reject this disturbance effectively.

As the second operating point considers a more challenging disturbance, it helps to distinguish ADRC controllers from one another. Consider the HOSM observer shown in pink. This observer quickly recovers to the setpoint but then proceeds to overshoot the setpoint and requires approximately 10 seconds to stabilise ($30 < t < 40$). By comparison the DOB (shown in red) correctly recovers to the setpoint with minimal overshoot velocity. This is due to its asymptotic stability properties. Finally, the ESO (shown in blue) overshoots with a degree of windup, causing the largest overshoot. This is then overcompensated for, causing the ESO to dip below the reference at $t = 32$. It can be concluded that the DOB has the best absolute performance, at the expense of requiring more information about the vehicle state, such as the velocity of the vehicle. For an observer which only requires minimal information, the HOSM observer has similar performance in disturbance recovery at the expense of some tracking error after recovery. Further designs which include more awareness of the overcentre state or disturbance profile may be able to smoothly control the vehicle trajectory.

The Overcentre mechanism can also be used to disturb state estimators, as an example consider Fig. 8 in which the top subfigure is the estimated position for the state estimation techniques considered (HOSM & ESO) and the bottom subfigure is the estimated velocity. The ground truth from the VICON system is shown in a solid line, the estimate is shown in a dashed line. Note that the performance of the HOSM is sufficient that the ground truth and estimated positions are barely distinguishable. Using Fig. 8 it can be concluded that the position estimation performance of the ESO is slightly degraded, however in this attached case the velocity estimation is not acceptable. By comparison, the HOSMO has excellent position estimation performance. The velocity estimation of the HOSM is significantly different to the ground truth data. Further experiments may be required to analyse factors affecting state estimation.

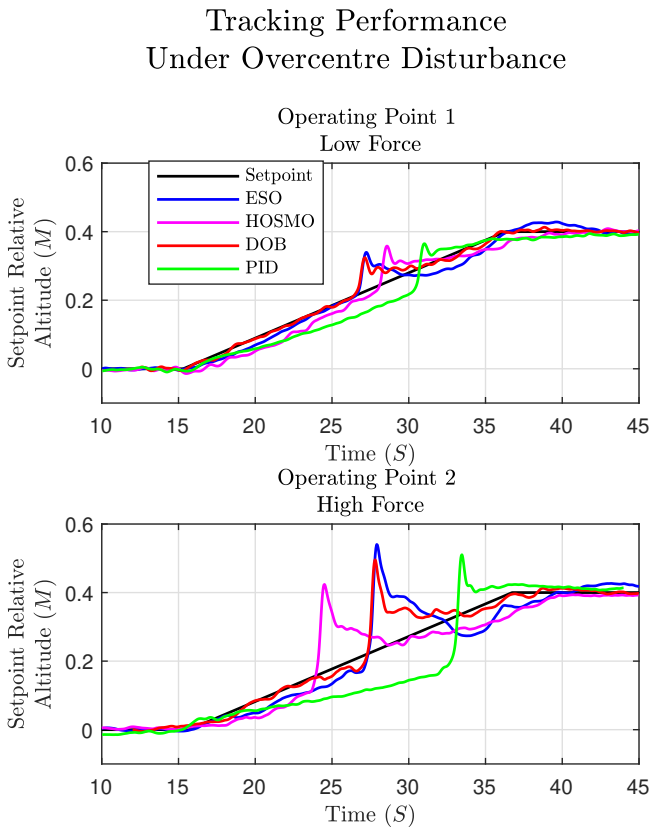

Fig. 7: Altitude response for the considered observers in two overcentre operating conditions.

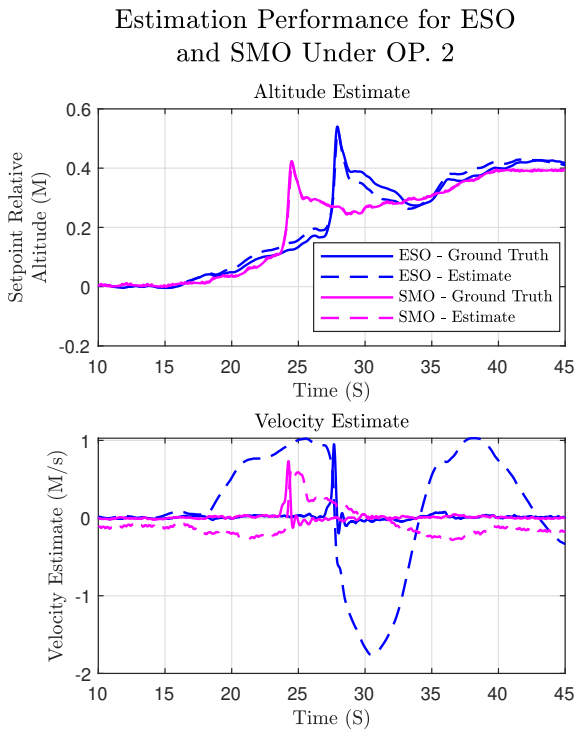

Fig. 8: Estimation performance of ESO and HOSM observers under operating point two. Note that the HOSM position estimate completely overlaps ground-truth data.

VI. Conclusions and Further Work

A new way of testing aerial manipulation controllers has been proposed using an overcentre mechanism to provide a switched disturbance to a UAV. This mechanism provides a tunable disturbance which can be positioned to excite altitude, position, or attitude dynamics. Following this, a Disturbance Observer; Extended State Observer; and Higher Order Sliding Mode Observer are tested with this unusual disturbance. Experiments are conducted at a low-force and high-force operating point. In both cases, the Disturbance Observer shows the lowest overshoot and mean square error at the cost of requiring additional state information. A Higher Order Sliding Mode Observer provides similar overshoot performance with marginally degraded tracking performance without requiring the full vehicle state. The Extended State Observer performance degrades severely in the higher force operating point. This shows that the overcentre mechanism is a suitable source of disturbance for experimentally testing different ADRC techniques. Its ability to be quickly modified to create more challenging disturbances has been demonstrated with two operating conditions. Additional work may include testing the overcentre mechanism in different orientations or positions, or the development of a model-based controller which aims to smoothly reject the influence of the mechanism based on knowledge of the disturbance profile.

References

[1] Gabriel Baraban et al. "Adaptive Parameter Estimation for Aerial Manipulation". In: *2020 American Control Conference (ACC)*. 2020, pp. 614–619.

[2] Federico Benzi et al. "Adaptive Tank-based Control for Aerial Physical Interaction with Uncertain Dynamic Environments Using Energy-Task Estimation". In: *IEEE Robotics and Automation Letters* 7.4 (2022), pp. 9129–9136.

[3] Hossein Bonyan Khamseh, Farrokh Janabi-Sharifi, and Abdelkader Abdessameud. "Aerial manipulation—A literature survey". In: *Robotics and Autonomous Systems* 107 (2018), pp. 221–235. ISSN: 0921-8890.

[4] Jeonghyun Byun et al. "Stability and Robustness Analysis of Plug-Pulling using an Aerial Manipulator". In: *2021 IEEE/RSJ International Conference on Intelligent Robots and Systems (IROS)*. 2021, pp. 4199–4206.

[5] Salua Hamaza et al. "Sensor Installation and Retrieval Operations Using an Unmanned Aerial Manipulator". In: *IEEE Robotics and Automation Letters* 4.3 (2019), pp. 2793–2800.

[6] Suseong Kim, Hoseong Seo, and H. Jin Kim. "Operating an unknown drawer using an aerial manipulator". In: *2015 IEEE International Conference on Robotics and Automation (ICRA)*. 2015, pp. 5503–5508.

[7] James Knowles, Bernd Krauskopf, and Mark H. Lowenberg. "Numerical continuation applied to landing gear mechanism analysis". In: (Sept. 2015).

[8] Dongjae Lee et al. "Aerial Manipulation using Model Predictive Control for Opening a Hinged Door". In: *2020 IEEE International Conference on Robotics and Automation (ICRA)*. 2020, pp. 1237–1242.

[9] Jaime A. Moreno. "Lyapunov function for Levant's Second Order Differentiator". In: *2012 IEEE 51st IEEE Conference on Decision and Control (CDC)*. 2012, pp. 6448–6453.

[10] Fabio Ruggiero, Vincenzo Lippiello, and Anibal Ollero. "Aerial Manipulation: A Literature Review". In: *IEEE Robotics and Automation Letters* 3.3 (2018), pp. 1957–1964.

[11] Yinshuai Sun et al. "A Switchable Unmanned Aerial Manipulator System for Window-Cleaning Robot Installation". In: *IEEE Robotics and Automation Letters* 6.2 (2021), pp. 3483–3490.

[12] Vibhu Kumar Tripathi et al. "Finite-time super twisting sliding mode controller based on higher-order sliding mode observer for real-time trajectory tracking of a quadrotor". In: (2020). ISSN: 1751-8644.

[13] Dimos Tzoumanikas et al. *Aerial Manipulation Using Hybrid Force and Position NMPC Applied to Aerial Writing*. 2020. URL: https://arxiv.org/abs/2006.02116.

[14] Mengxin Xu, An Hu, and Hesheng Wang. "Image-Based Visual Impedance Force Control for Contact Aerial Manipulation". In: *IEEE Transactions on Automation Science and Engineering* (2022), pp. 1–10.